HHS Public Access

Author manuscript

*IEEE Trans Biomed Eng*. Author manuscript; available in PMC 2018 November 06.

Published in final edited form as:

*IEEE Trans Biomed Eng*. 2017 November ; 64(11): 2595–2606. doi:10.1109/TBME.2016.2644651.

# *In situ* mechanical characterization of multilayer soft tissue using ultrasound imaging

**Saurabh Dargar [graduate student]**,
Biomedical Engineering Department and with the Center for Modeling, Simulation and Imaging in Medicine (CeMSIM) at Rensselaer Polytechnic Institute in Troy, NY, USA. dargas@rpi.edu.

**Ali C. Akyildiz [postdoctoral researcher]**, and
Center for Modeling, Simulation and Imaging in Medicine (CeMSIM) at Rensselaer Polytechnic Institute in Troy, NY, USA. akyila@rpi.edu.

**Suvranu De [Director, Head]**
CeMSIM; Department of Mechanical, Aerospace and Nuclear Engineering (MANE) at Rensselaer Polytechnic Institute in Troy, NY, USA. des@rpi.edu.

## Abstract

In this paper we report the development of a technique to characterize layer-specific nonlinear material properties of soft tissue *in situ* with the potential for *in vivo* testing. A Soft Tissue Elastography Robotic Ann (STiERA) system comprising of a robotically manipulated 30 MHz high-resolution ultrasound probe, a custom designed compression head and load cells has been developed to perform compression ultrasound imaging on the target tissue and measure reaction forces. A multi-layer finite element model is iteratively optimized to identify the material coefficients of each layer. Validation has been performed using tissue mimicking agar-based phantoms with a low relative error of ~7% for two--layer phantoms and ~10% error for three layer phantoms when compared to known ground-truth values obtained using a commercial material testing system. The technique has then been used to successfully determine the *in situ* layer-specific mechanical properties of intact porcine stomach. The mean $C_{10}$ and $C_{20}$ for a second order reduced polynomial material model were determined for the muscularis (6.41±0.60, 4.29±1.87 kPa), submucosal (5.21±0.57, 3.68±3.01 kPa) and mucosal layers (0.06±0.02, 0.09±0.24 kPa). Such a system can be utilized to perform *in vivo* mechanical characterization, which is left as future work.

### Keywords

Biomechanics; Medical simulation; ultrasonic imaging

## I. Introduction & Background

THE tissues of each organ can be structurally classified based on the morphology of its comprising parts, such as the distinct layers of the skin (dermis and epidermis), gastrointestinal track (mucosa, submucosa and muscularis) or arteries (adventitia, media and intima). The overall mechanical behavior of each of these tissues is dependent on the material property of each individual layer. In order to model the mechanical behavior of such

tissue, we require layer-specific characterization. Modeling multilayer tissue behavior can be useful in better understanding tissue healing and remodeling [1], mechanosensing [2] and developing realistic virtual reality simulators for surgical procedures such as natural orifice transluminal endoscopic surgery (NOTES) [3], [4] or endoluminal procedures such as endoscopic submucosal dissection (ESD) [5], [6] that involve tunneling between layers.

Traditionally, the mechanical characterization of multilayer tissues has been performed by considering the entire thickness of the tissue as a homogenous material and assigning an appropriate material model. In particular, the esophagus has been studied extensively to determine bulk properties by performing inflation experiments and observing dilation using ultrasound imaging [7]–[12]. Takeda et al. were able to perform esophageal dilation experiments on humans using a compliant balloon structure and an ultrasound probe to determine the tissue wall stress during dilation [13]. Similar studies assuming the tissue as a homogenous material have also been performed on the intestines [14]–[16], skin [17]–[21] and arteries [22]–[26]. Yassi et al. developed an anatomically realistic 3D simulation of the gastroesophageal junction [27]. During simulations they noted deviations from experimental data due to the unavailability of constitutive models capable of explaining the muscular layer behavior, highlighting the need for layer-specific models.

Layer-specific mechanical properties of a variety of soft tissues such as intestines, arteries and skin have also been described. These testing techniques can be classified distinctly into methods that study the tissue *in situ/in vivo* or *ex vivo. Ex vivo* studies characterize the tissue outside its natural anatomical and physiological context and might not maintain the structural integrity of the layers by testing them separately. Comparatively, *in situ* studies are performed on the whole organ and maintain the layered structural integrity but not necessarily the *in vivo* physiological conditions.

In many gastrointestinal tissues, such as the stomach and esophagus, the morphology of the tissue allows the surgical separation of the mucosal and muscularis layers with relative ease. This has allowed a variety of *ex vivo* studies to be performed on stomach [28], [29] and esophagus [30]–[34] where the layers are tested separately. While these tests allow each individual layer to be tested in their no-load states, the degree of tissue damage imparted in surgical separation is unknown and fails to acknowledge the impact of layer-layer bonding on the overall tissue behavior. Also, in gastrointestinal tissue, there are more layers than the two easily separable mucosal and muscularis layers, such as the mucosa and submucosa, which cannot be surgically separated with precision and such techniques consider the two mucosal layers as one. Many *ex vivo* layer-specific studies have been performed previously while keeping the multi-layer tissue intact. The esophagus [35]–[37] intestines [38], [39], skin [17], [40], [41] and stomach [42], [43] have been tested in detail. However, excising small segments of the organ for inflation, uniaxial or biaxial testing imparts an unknown degree of tissue damage and is still unrepresentative of the *in situ* state of the organ.

Thus, in order to measure the most anatomically and physiologically relevant layer-specific material properties of multilayer tissue, we require a testing method capable of maintaining the structural integrity of the tissue while testing the layers *in situ* and eventually *in vivo*. Prior studies have shown that there are significant differences in material properties of soft

tissue when tested in vivo/in situ vs. ex-vivo [44]–[46], attributed to loss of perfusion, onset of muscular rigor mortis and relaxation of internal residual stresses/strains. Ultrasound based quantitative compressive elastography is a viable technique to subject the tissue to a loading regime while non-destructively visualizing layer-specific behavior of tissue. Elastography is a method employing the use of ultrasound imaging to quantitatively visualize the deformation, and eventually the elastic modulus distribution of tissue while under an external load, typically compression [47]. Elastography has been previously used to study the layer-specific and bulk mechanical properties of multi-layer soft tissues, such as blood vessels [48], articular cartilage [49], skin [50] and breast tissue [51]. The use of ultrasound allows for the strain field of each layer to be visualized without having to strip layers apart, be it is *in situ* or *in vivo*. This ability to test the tissue and maintain the *in situ* configuration of the tissue layers without the need to excise sections of tissue from the organ distinguishes compression elastography from the aforementioned techniques. Even in inflation testing which can be performed *in vivo*, there is limited to no control over the boundary conditions of the inflated organ, making quantitative inferences from the elastography results uncertain. Also, for an *in situ* technique to have *in vivo* feasibility it must be able to access the organ *in vivo* and then perform the compression sequence with precision. Using a programmable robotic arm capable of executing precise loading regimes allows the elastography compression head to be placed on the target organ. Handheld compression elastography has been performed and tested in the past [52]–[55], however the unreliability of the handheld loading rate and the orientation of the organ-to-probe contact have been cited as reasons for uncertainty in the quantitative results.

In this work we have developed both a hardware and software framework capable of characterizing layer-specific material properties of soft tissue *in situ* with *in vivo* testing feasibility. The hardware consists of a robotic arm that supports the ultrasound probe and allows precise deformation of the organ, while at the same time, measuring indentation force using a six-axis sensor. In the remainder of this paper, we refer to this system as the Soft Tissue Elastography Robotic Arm (STiERA). A finite element-based computational model is utilized to identify layer-specific material properties based upon an optimization algorithm. In this paper we report studies using multilayer agar gel specimens as well as *ex vivo* porcine stomach tissue.

## II. Methods & Materials

### A. Soft Tissue Elastography Robotic Arm (STiERA) hardware

Our Soft Tissue Elastography Robotic Arm (STiERA) hardware system is a robotically manipulated elastography compression testing instrument, composed of a robotic arm and a custom designed compression head mounted on the arm (Fig.1). The six-degrees-of-freedom robotic arm (UR5, Universal Robots) provides accurate positioning of the compression head in 3D and precise loading speed in the compression experiments. The robotic arm has the ability to be programmed for variable compression rates between 0.1 mm/s and 1000 m/s. A custom designed compression head fixture was attached to the end-effector of the robotic arm. The fixture is instrumented with two load cells (ATI nano17 precision), which provides real-time load data at 1000 Hz with a resolution of 0.0125 N.

The compression head encapsulates a high frequency ultrasound probe (Ultrasonix L40-8/12 linear array probe) operated at 30 MHz (bandwidth 20 MHz) consisting of 128 elements with a 100 micron element pitch, a focal range of 2 to 30 mm (8mm elevational focus) and an expanded imaging width of 16 mm, providing a 14 micron axial and 25 micron lateral resolution. This particular probe frequency was chosen in order to attain sufficient intra-layer resolution. Previous studies have shown the porcine stomach muscularis and submucosa-mucosal layers to be 3-4 mm in thickness [28], [56] with the submucosa being a much thinner component of the mucosal-submucosal combined layer. With a 30 MHz probe operating frequency we anticipate to visualize ~70 pixels per mm of gastric tissue, providing substantial layer-specific information. The images are recorded and displayed on the Ultrasonix Sonixone portable ultrasound unit with a variety of post processing capabilities. The ultrasound probe images the target tissue underneath through a small aperture in the circular compression head, where the compression head has a diameter of 38 mm. Since the surface of the ultrasound probe sits flush with the surface of the compression head, it ensures a uniform compression surface.

## B. Computational modeling

Most biological materials exhibit varying degrees of anisotropy, inhomogeneity and are nearly incompressible materials which may experience large deformations under *in vivo* loading conditions. These biological materials can be considered rate independent at low strain rates making such material great candidates for modeling using hyperelasticity.

Thus in order to model the target material, an appropriate hyperelastic material model needs to be identified. For our purposes we assumed the material to be isotropic, incompressible and homogenous. Four hyperelastic models, presented in Table 1 were evaluated, which included the 1) Neo-Hookean, 2) Mooney-Rivlin, 3) a second order reduced polynomial, and 4) the Yeoh model. Table 1 also presents the Cauchy stress in terms of the principal stretch for uniaxial unconfined compression testing. Here $\lambda_1$ is the corresponding principal stretch for the isotropic uniaxial compression case with $\lambda_1 = 1 - d/h$ wherein 'd' is the displacement of the compression head and 'h' is the initial uncompressed height of the sample where $\lambda_1$ is related to the other 2 principal stretches by $\lambda_1 = 1 \Big/ \lambda_2^2 = 1 \Big/ \lambda_3^2$. Here $I_1$ and $I_2$ are the first and second invariants of the strain tensor, defined as, $I_1 = \lambda_1^2 + \lambda_2^2 + \lambda_3^2$ and $I_2 = \lambda_1^2\lambda_2^2 + \lambda_2^2\lambda_3^2 + \lambda_3^2\lambda_1^2$. In these models, the $C_{10}$, $C_{01}$, $C_{20}$ and $C_{30}$ parameters are the material coefficients.

The identification of the optimal material parameters of multilayer biological material is an optimization problem, wherein the material coefficients of the material law are iteratively updated in the finite element model so as to minimize the difference between the experimental and simulated force and displacement data. Based on studies presented in section 3.1, we have chosen the second order reduced polynomial model for both computational efficiency and accuracy.

Thus, to determine the optimal material parameters for each of the tissue layers, a finite element model of the multilayer tissue was developed and the following objective function,

representing the difference between the model predictions and experimental observations, was iteratively minimized:

$$p(\overrightarrow{C}) = \sum_{i=1}^{n}\left[w_1\left(\sum_{j=1}^{m-1}\left[d_{ij}^{s}(\overrightarrow{C}) - d_{ij}^{e}\right]^2\right) + w_2\left(f_i^{s}(\overrightarrow{C}) - f_i^{e}\right)^2\right] \quad (1)$$

In this equation, layer-specific coefficients are stored in the vector $\overrightarrow{C}$. Here $d_{ij}$ is the axial displacement of a point located at the interface of layers 'j' and 'j+1', along the axis of symmetry of the specimen at time point 'i' where 'n' is the total number of time points and 'm' is the total number of layers. A layer is defined as a morphologically distinct and mechanically distinguishable region of the tissue with its thickness along the compression direction of the probe. For the agar gel experiments reported next, the layers are intentionally prepared to have distinct mechanical properties. For the stomach tissue, the boundaries between layers is determined using ultrasound B-mode images (Figure 8) and each layer is assumed to have homogenous material properties. Superscripts 'e' and 's' denote experimental and simulated data, respectively, $f_i$ is the axial force on the indenter at time point 'i' In the objective function, the displacement and reaction force were weighted equally such that $w_1 = w_2 = 0.5$. Previous work has shown that in a 2D incompressible inverse problem, the elastic modulus can be reconstructed almost uniquely with only 2 displacement fields and uniquely with four, without any knowledge of the boundary conditions [57]. For our computations, we have used n=6 isotemporal time points along with the boundary condition for each displacement field, thus making the problem better posed to yield a unique set of optimal material parameters $\overrightarrow{C}$. Figure 2 is a flowchart showing the algorithm for the iterative optimization routine used to identify the optimal material coefficient vector.

The 'trust-region-reflective' optimization method [58], extensively applied to soft tissue finite strain applications [59]–[61], has been employed in this work. Though the Levenberg-Marquardt algorithm has also been used extensively in soft tissue finite strain material coefficient optimizations [62]–[64], it has known limitations for negative definite Hessian matrices [65], which are overcome when the trust-region-reflective optimization is used. The trust-region-reflective algorithm was implemented by means of the Matlab® curve fitting toolbox, which iteratively modified the material model coefficients and subsequently altered the Abaqus simulation input file for finite element simulations. The input parameters for the trust-region-reflective algorithm in Matlab® were set as per Table.2.

### C. Mechanical characterization of agar gel phantoms using STiERA

In order to test the accuracy of the ultrasound-based material characterization method, a test protocol involving single and multi-layered tissue mimicking agar gel samples was designed allowing the comparison of material properties obtained from a commercial, validated material testing system (MTS) to the results obtained from the STiERA based system. Such agar gel samples have been shown to be good substitutes for soft tissue elastography [66]–[68].

**1) Preparation of single-layer and multi-layer agar gel test samples—**Three master batches of agar gel concentrations were prepared from gelatin (8% weight/volume), psyllium fiber (1% weight/volume) and varying concentrations of agar (1%, 2.5% and 4% weight/volume). The agar concentration modulated the stiffness, the gelatin allowed the gel to set and the psyllium fiber provided echogenic contrast in the samples for ultrasound imaging. The master batches were prepared by melting the agar mixture in a microwave which was then poured into 150 mm long cylindrical molds with a diameter of 34 mm and left to set for 6 hours at room temperature. From each of the three master batches, three 10 mm thick discs were cut to yield the single layer test samples. In total, nine single-layer samples were obtained for MTS testing.

The multi-layer (two-layer and three-layer) test samples were assembled from the same 4%, 2.5% and 1% concentration agar gel master batches, as shown in Figure 3. Three 3 mm thick discs were sliced from each concentration of agar gel master batch to ensure physiologically relevant layer thickness [28], The layers were glued to each other by pipetting 2 ml of warm 8% weight/volume gelatin between the interfaces and then kept in the fridge for 120 seconds in order to set. Three two-layer and three three-layer test samples were prepared for compression tests with STiERA.

**2) Compression testing and characterization of single-layer samples with Instron® MTS—**The objective of testing single layer samples was to determine which one of the four hyperelastic material models listed in Table 1 was best capable of capturing the behavior of the different concentrations of agar samples while under unconfined compression testing on the Instron® MTS system. In order to identify the mechanical properties of each of the three agar gel concentrations, single-layer samples with 4%, 2.5% and 1% agar concentrations were tested on the Instron® MTS system. Each of the single-layer samples was coated with 5 ml of generic vegetable oil on the top and bottom surfaces before being placed between the uniaxial compression head apparatus on the Instron® MTS, to ensure frictionless boundary conditions for the unconfined compression test. The samples were compressed up to a maximum compression of 20% at a loading speed of 0.1 mm/s. Each test was repeated three times (27 tests in total). Displacement of the compression head and the load applied on the samples were recorded during testing.

**3) Compression testing & ultrasound measurements with STiERA—**The multi-layer samples were placed onto the experimentation stage of the STiERA for compression testing. The lower boundary was glued to the surface to impose an encastered boundary condition while the top surface was coated with a thin layer of 5 ml of vegetable oil to provide a frictionless boundary condition. In similar fashion to the compression of the single layer samples, the STiERA system was programmed to compress the multi-layer samples by 20% of the total composite thickness at a loading speed of 0.1 mm/s. Each multi-layer sample was tested three times (18 tests in total). Figure 4 shows a typical force signal obtained from 20% compression of 2 and 3-layer agar gel samples.

The ultrasound system (Ultrasonix SonixOne) was used to record B-mode video sequence, which provides a high-resolution video sequence of the subsurface target material while undergoing compression. The B-mode images constructed by the system were used to

estimate the displacement instead of RF data because the B-mode image reconstruction algorithm developed by the manufacturer was optimized for the transducer array and provided sufficient layer-specific resolution for our target tissue. The B-mode video sequence was then down-sampled to 3 Hz in order to ensure a minimum of 25 micron displacement between consecutive frames since the resolution of the probe was 14 microns axial and 25 microns lateral. Deformation of the tissue during compression testing was acquired by computing the displacement field between two consecutive isotemporal B-mode images with an open-source, intensity based image registration toolkit known as *elastix* [69]. Once the displacement field between consecutive B-mode images was calculated using *elastix*, the total displacement field was calculated in Matlab® by vector addition (Lagrangian displacement). Note that there is no necessity to compute the strain fields explicitly from the experimentally observed displacement fields.

Finite element models of the multilayer agar gel samples were created using the commercial software package Abaqus (Dassault Systemes Simulia Corporation, Providence, Rhode Island, USA). The test samples had uniform layer thicknesses and were cylindrical in shape, thus an axisymmetric model was implemented for the simulation. The lower boundary of the test sample was encastered using glue while the top boundary was set to a frictionless contact with the indenter surface. The mesh was created with a seed size of 0.1 mm, thus for a sample with a thickness of 9 mm and with a diameter of 30 mm, the model contained a total of ~10,500 elements with ~8000 linear quadrilateral elements (CAX4RH) elements.

**4) Layer-specific solution sensitivity of the agar gel sample—**In order to interpret the results from the agar gel experiments, it was critical to understand the sensitivity of each coefficient and its respective impact on the overall accuracy of the solution. Sensitivity maps were generated by modulating the coefficients of the chosen model and compared to the ground-truth by plotting the error for each combination of the model coefficients.

### D. Mechanical characterization of layer-specific properties of porcine stomach wall ex vivo

Once the accuracy of the STiERA for measuring mechanical properties was established using the agar gel phantoms, it was used to identify the layer specific properties of porcine gastric tissue. Porcine stomachs from pigs weighing ~115 kg were sourced from a local slaughterhouse and tested using the STiERA system within 5 hours post-mortem and staged identically to the multi-layer agar gel testing setup. The porcine stomach was cut open along the lesser curvature to expose the inner surface of the stomach. Once flattened out, the stomach was placed onto the staging platform already covered with a 120 grade commercial sandpaper (115 micron particle diameter) to provide a very high friction surface to experimentally impose a non-slip boundary condition. The top surface of the gastric tissue was coated with a thin layer of 15 ml of vegetable oil to provide a surface of minimal friction as was done for the agar gel phantoms. In similar fashion to the compression of the agar gel phantoms, the STiERA system was programmed to compress the multi-layer samples to a maximum compression of 20% at a loading speed of 0.1 mm/s. A total of 4 porcine stomachs were tested at two distinct locations on both sides of the organ (four

locations per stomach in total). Each location was tested three times with a wait time of 3 minutes between successive tests to allow the tissue to relax to its initial configuration.

The finite element models of the porcine gastric tissue were generated with the assumptions of axisymmetry, incompressibility and isotropy. The thickness of each layer was identified using the pre-compression B-mode ultrasound images and reflected in the finite element model geometry. The one fundamental difference in this case was the introduction of edge effects between the compression head and the tissue since the tissue domain was larger than the compression head. The gastric tissue was modeled as a semi-infinite medium by making the diameter of the soft tissue at least six times greater than the compression head to avoid any boundary effects on the displacement field. All other finite element parameters including seed size and objective function minimization parameters were kept the same. In figure 5 we can see the tissue layer geometries along with the created mesh.

## III. Results

### A. Testing with agar gel specimens

Prior to developing the material models for the agar gel samples, it was necessary to compare the force-strain curves between the Instron® MTS and STiERA systems. A comparison of the force-strain curves from the two systems yielded ~2.2% relative error in force when 4%, 2.5% and 1% single layer agar samples were tested. In figure 6 we can see the comparison between the two systems for the single layer 2.5% agar concentration sample.

The load-displacement data from each of the single-layer Instron® MTS experiments was used to calculate the experimental stretch and stress values, and then each of the four material models listed in Table 1 were fit to the experimental data using the Matlab® curve fitting toolbox. The curve fitting yielded the model-specific material coefficients along with the root-mean-square-error (NRMSE) of each material model, which was then normalized to the range of stress, as shown in equation 2. Here $\sigma_{e,i}$ and $\sigma_{m,i}$ are the experimental and model predicted stress values for the time point ‘i’ where ‘n’ is the number of data points in the experimental data set. Using the NRMSE value, the model with the lowest percentage error was identified and implemented to determine the ‘ground-truth’ coefficient values for each respective agar gel concentration.

$$NRMSE = 100^{*}\frac{\sqrt{\sum_{i=1}^{n}\left(\sigma_{e,i}-\sigma_{m,i}\right)^{2}/n}}{\left(\sigma_{e,\max}-\sigma_{e,\min}\right)} \quad (2)$$

Figure 7 is a representative example comparing the ability of the four models to capture the behavior of the 2.5% concentration single-layer agar gel sample. The experimental data exhibits strain stiffening with increasing compressive strain. The difference in performance of each model is evaluated by means of the NRMSE. Table 3 provides the model error values of all four models for each of the three agar gel concentrations. The results in Table 3

show that the 2nd order reduced polynomial and Yeoh model show the least NRMSE values, and outperform the Neo-Hookean and Mooney-Rivlin models. In the remainder of the study the 2nd order reduced polynomial model has been used as it involves just two parameters ($C_{10}$ and $C_{20}$).

Table 4 shows the material parameter values of the 2nd order reduced polynomial material model. The results indicate that with an increasing concentration of agar there is an increase in the stiffness of the sample, as expected. As the agar's weight per volume of sample is increased from 1% to 4%, we see an increase in the $C_{10}$ parameter from 2.10 ±0.05kPa to 12.70 ±0.48kPa.

Prior to determining the layer-specific material parameters of the multi-layer agar gel samples, displacement fields were calculated for each of the 2 and 3-layer agar gel samples using *elastix*. Figure 8(c) shows the displacement field at 20% compression obtained from a representative 3-layer agar gel sample using the pre and post compression isotemporal ultrasound B-mode images. The B-mode images are able to clearly illustrate the three agar gel layers.

In order to compare the results obtained from the STiERA based system to the ground-truth values, we directly compared the coefficient values and also calculated the % relative error between the strain energies of the ground-truth and STiERA system based model.

For the 2-layer agar gel samples, the STiERA based system determined a mean $C_{10}$ value of 12.5±1.0 kPa (ground-truth 12.7 kPa) and $C_{20}$ value of 3.0±2.9 kPa (ground-truth 2.1 kPa) for layer 1 with a 0.43% relative strain energy error. The $C_{10}$ and $C_{20}$ for layer 2 were 2.1±0.7 kPa (ground-truth 2.1 kPa) and 5.3±5.6 kPa (ground-truth 3.1 kPa) with 13.9% relative strain energy error. The variation in $C_{20}$ appears to be high, however the low % relative strain energy error for each layer indicates a good fit. Figure 9(a) further illustrates that the layer-specific models determined using STiERA were able to capture the ground-truth stress-stretch behavior fairly well. The ground-truth stress-stretch response curves were plotted using the ground-truth $C_{10}$and $C_{20}$ parameters identified from the mechanical characterization of single layer agar gels using the Instron MTS® experiments.

Testing on the 3-layer agar gel samples using the STiERA yielded mean $C_{10}$ and $C_{20}$ values of 11.9±0.4 kPa (ground-truth 12.7 kPa) and 3.5±2.6 kPa (ground-truth 2.1 kPa) for layer 1 with a 4.7% strain energy error as shown in figure 9(b). The mean $C_{10}$ and $C_{20}$ values for layer 2 were 5.2±0.5 kPa (ground-truth 5.1kPa) and 9.5±6.7 kPa (ground-truth 14.03 kPa) with a 6.3% relative strain energy error. Lastly the mean $C_{10}$ and $C_{20}$ values for layer 3 were 2.5±0.3 kPa (ground-truth 2.1 kPa) and 4.0±2.0 kPa (ground-truth 3.1 kPa) with a 18.5% relative strain energy error. Once again, the $C_{20}$ parameter shows significant degree of variation, however the % relative strain energy error for each layer indicates a good fit to the ground-truth stress-stretch response curves.

Finally, we also performed an error analysis on the results obtained from the optimization method. We define two error measures by discretizing the 2-layer sample using 16 nodes and the 3-layer sample using 22 nodes along the axis of symmetry and observing the displacements at those nodal points at six isotemporal time points from the compression

sequence which were then used in the optimization method. In figure 10(a) we show the % relative displacement error as a function of time defined by the following equation:

$$\varepsilon_d(i) = 100^* \frac{\sqrt{\sum_{j=1}^{m} \left(d_{ij}^s - d_{ij}^e\right)^2}}{\sqrt{\sum_{j=1}^{m} \left(d_{ij}^e\right)^2}} \quad (3)$$

where '$d_{ij}$' is the displacement of node 'j' at time point 'i' and 'm' is the total number of nodes along the depth of the sample. Superscripts 'e' and 's' denote experimental and optimized parameter simulated data, respectively. The results indicate that for the representative samples shown, the relative error remains within 2.5% over the course of the six time points. In figure 10(b) we present the % relative displacement error at the nodal points along the depth of the sample defined by the following equation:

$$\varepsilon_d(j) = 100^* \frac{\sqrt{\sum_{i=1}^{n} \left(d_{ij}^s - d_{ij}^e\right)^2}}{\sqrt{\sum_{i=1}^{n} \left(d_{ij}^e\right)^2}} \quad (4)$$

where 'n' is the total number of time points used in the computations (n=6). The plots show that the maximum relative displacement error is ~2.75% with the error reducing from the top of the sample towards the bottom. These two plots provide further confidence in the chosen material constitutive law and the optimization algorithm.

## B. Layer-specific solution sensitivity of the agar gel samples

The coefficient sensitivity maps were evaluated for each of the three agar gel concentrations, as shown in Figure 11. They were calculated by computing the strain energy using Abaqus for each combination of $C_{10}$ and $C_{20}$ between 1 and 30 kPa for up to 20% compressive strain. The strain energy at each $C_{10}$ and $C_{20}$ combination was compared to the ground truth parameters to yield the relative % error. These maps highlight the accuracy of the solution in response to any change in the $C_{10}$ and $C_{20}$ coefficients (in kPa). The sensitivity maps in Figure 11 have been scaled to show % relative strain energy error of only 20% or less. Thus, any combination of $C_{10}$ and $C_{20}$ values within the color map captures the ground-truth material properties with an error of 20% or less. For example for layer 2 in Figure 11, varying the ground truth $C_{20}$ value of 14.01 kPa by 10 kPa will still yield a solution with an error of 20% or less. However for the $C_{10}$ coefficient of 5.1kPa, a variation of 10 kPa will yield a solution with a relative % error of greater than 20%. A similar observation can be made about layers 1 and 3, where the $C_{20}$ coefficient is much more tolerant to changes than the $C_{10}$ coefficient while keeping the error below 20%.

## C. Ex vivo porcine stomach

Once the system was validated for its ability to identify the material coefficients of multi-layer agar gel constructs, the system was used to identify the material coefficients of the muscularis, submucosa and mucosal layers of *ex vivo* porcine stomach tissue. Using the

STiERA system three distinct layers of gastric tissue, the muscularis, submucosa and mucosa layers were visualized and the displacement fields were obtained successfully (Figure 12). The pre-compression B-mode ultrasound images were used to evaluate the thickness of each layer and were determined to be 2.36±0.31 mm, 0.74±0.10 mm and 2.97±0.19 mm for the muscularis, submucosa and mucosal layers, respectively. Similar morphometric results were obtained by Zhao et al [29] who reported the thickness of the muscularis and the combined mucosa-submucosa as 4mm and 3 mm (3.71 mm in our case), respectively for pigs weighing 100kg. Jia et al [28] also reported similar results for the serosa-muscle (~2.9 mm) layer and combined mucosa-submucosa (~2.9 mm) layer for pigs weighing 140kg. Figure 13 shows the mean and the range of stress-stretch behavior of the porcine stomach wall layers identified with the STiERA system. The results showed the presence of strain stiffening for all three layers, primarily at stretch ratios beyond 0.88. For all four stomach samples tested, the muscularis layer was the stiffest with a mean $C_{10}$ value of 6.41±0.60 kPa and a mean $C_{20}$ value of 4.29±1.87 kPa (Table 5). The submucosal layer appeared to be slightly more compliant with a $C_{10}$ value of 5.21±0.57 kPa and a $C_{20}$ value of 3.68±3.01 kPa. The mucosal layer was identified to be significantly more compliant than the other two layers with a $C_{10}$ value of 0.06±0.02 kPa and a $C_{20}$ value of 0.09±0.24 kPa. The plots in Figure 13 also highlight the uncertainty in the experimentally obtained models. This uncertainty is difficult to judge solely by the mean and standard deviation of the $C_{10}$ and $C_{20}$ coefficients, however, the size of the colored patches in Figure 13 showcase the uncertainty better.

## IV. Discussion

In this work we presented an elastography-based technique to characterize the layer-specific nonlinear mechanical properties of multi-layer tissues without compromising tissue integrity. Our goal is to develop an understanding of layer-specific tissue behavior under large deformation, which is useful for developing surgical simulators and understanding tissue healing and remodeling. since soft tissues are known to exhibit nonlinear behavior in the large deformation regime [70], our method was designed to elicit the nonlinear mechanical response of the tissue by compressing the tissue up to 20%, well beyond the 10% nominal strain linear regime [71], [72]. The technique was validated with a series of experiments on tissue-mimicking muti-layer agar gel samples and then further used to identify the mechanical properties of intact porcine gastric wall layers *ex vivo*.

The ground truth for the mechanical behavior of agar gel samples of different concentrations was established by testing the single layer samples with a commercial compression testing setup and analyzing the performance of four hyperelastic material models. Neo-Hookean models have been implemented for agar gel before [73][67], however the success of this single parameter model is largely limited to the nearly linear elastic region of the material, typically under 10% compression [67]. As it was also observed in our study, it fails to characterize the non-linear, strain stiffening behavior in the large deformation region accurately (4.77% error). The Mooney-Rivlin model was able to provide an improvement upon the Neo-Hooken model by capturing the non-linearity slightly better (2.44% error). The 2$^{nd}$ order reduced polynomial model and Yeoh model represented the nonlinearity and strain stiffening in the experimental data the best with a low error of 1.11%. As the 2$^{nd}$ order

reduced polynomial model has fewer coefficients and hence, computationally less expensive in the optimization procedure, it was chosen as the material model for finite element modeling of multilayer samples.

After establishing the ground truth for mechanical properties of agar gel samples, the developed material characterization method was validated by comparing its results to the ground truth and quantifying the % relative strain energy error. The 2-layer agar gel tests showed satisfactory fit results with 0.43% and 13.9% relative strain energy error for layer 1 and layer 2, respectively. Similarly, the 3-layer sample tests also low relative error values: 4.7%, 7.31% and 18.5% for the top, middle and bottom layer, respectively. Here, a general trend can be isolated where the layer proximal to the ultrasound probe has a better model fit as compared to the distal layers. The decrease in model fit for a layer further away from the probe can be attributed to the introduction of errors due to the ultrasound imaging and displacement estimation using *elastix*. It is known experimentally that the accuracy of ultrasound measurements decrease as a function of depth [74], in particular higher frequency probes suffer from greater attenuation [75] also reducing accuracy. For example, in the 2-layer samples we can expect to see an increase in ultrasound measurement error as we move from layer 1 (top) to layer 2 (bottom), impacting the accuracy of layer 2 greater than layer 1. This indicates that layers proximal to the probe are impacted less by the ultrasound error as compared to the distal layers. The same trend can be observed in the 3-layer agar gel samples as well, where the proximal layer results are better (4.7% error) than the two distal layers (7.31% and 18.5%).

Also, these errors are attributable to the estimation error introduced by the image registration technique. In particular, image registration benchmarking studies on lung CT data using *elastix* showed and average error of 0.006% for high intensity boundary features and 0.5% for interior regions [76]. With the *elastix* benchmarking studies in mind we can also expect some error in the displacement fields, which can eventually impact the optimized material parameters.

Yet, despite the shortcomings observed in the modeling of the distal layers, the method performed satisfactorily as demonstrated by relative error values of below 20%. Although the data presented shows relative strain energy errors of less than 20% we still observed variation in the $C_{20}$ parameter. A deeper look at the sensitivity of the overall solution as a function of the material coefficients allows us to better understand the variation in the experimentally identified $C_{10}$ and $C_{20}$ parameters. For example, in layer 2 for the 3-layer agar gel sample, we can see that the mean $C_{10}$ coefficient is 5.2 kPa with a standard deviation of 0.5, however the $C_{20}$ coefficient has a mean of 9.5 kPa and a standard deviation of 6.7 kPa. The same pattern of variability in the $C_{20}$ parameter can be observed across other layers as well, for agar gels and *ex vivo* tests. However, the results consistently show errors of less than 20% quantified in terms of strain energy error, and as low as 0.43%, despite this $C_{20}$ variability. This illustrates that $C_{20}$ variability does not impact the modeled mechanical behavior as drastically as the $C_{10}$ parameter, which can be seen in the sensitivity maps (Figure 11). The results of the agar gel based validation experiments highlight that, despite the presence of displacement estimation uncertainty as well as any variability in the $C_{20}$ parameter, our system was consistently able to show satisfactory model fits. Also, the system

was consistently able to identify the correct ordering of each of the layers for both 2 and 3 layer samples highlighting the qualitative nature of the data obtained using the system.

The results from the *ex vivo* experiments indicated strain stiffening for all three layers beyond a stretch ratio of 0.88, hence a transition from a linear mechanical behavior to a non-linear one, as expected for biological soft tissues. The quantitative *ex vivo* results showed that the muscularis and submucosal layers are only slightly different in their overall stiffness. Although the muscularis was consistently stiffer than the submucosa, two samples (Figure 13 (a) and (c)) showed slight overlap in the mechanical behavior of the two layers above 10% of compression. This highlights that the two layers may almost equally contribute to the overall stomach wall stiffness while under compression in the larger finite compressive strain region (greater than 10%). The mucosal layer was determined to be the most compliant component of the gastric wall under compression. This layer is composed of the epithelium, lamina propria and a thin layer of muscularis mucosae [77], and in comparison to the muscularis and submucosal layers, contains significantly less amount of collagen, elastin and smooth muscle cells, which are responsible for contributing stiffness to the respective layers. Moreover, the mucosal layer consists of gastric glands with the appearance of a honeycomb structure. These tubular glands are secretory glands and do not allow a great degree of mechanical rigidity and contribute to the layers low stiffness.

A limitation of this study is that the modeling does not take into account the anisotropy of the layers. It is also known that soft tissues exist under pre-stresses in the *in vivo* condition and must be experimentally quantified in order to enhance the robustness and *in vivo* validity of the soft tissue models. Similarly, in this work we did not address the inhomogeneity in the porcine gastric tissue. It has been shown that the material properties of rat and rabbit gastric tissue is dependent on the location of testing and require and we anticipate similar inhomogeneous behavior in the porcine stomach [56]. These issues are left for future investigations.

## V. Conclusion

In this work we presented a technique to identify the layer-specific material properties of intact multi-layer tissues. The advantage of this system is that it is amenable to *in vivo* application. Validation of the system has been performed by compression loading experiments on agar gel phantoms and then used to identify layer-specific properties of *in situ* porcine gastric tissue. With a validated system capable of providing results with and average relative strain energy error of ~7% for two layer constructs and an average of ~10% error for three layer constructs, the framework was deemed capable of providing reliable layer-specific material properties in a non-destructive manner. The system was then used to identify the *in situ* layer-specific properties of porcine gastric tissue. A total of 4 porcine samples were tested in 4 locations successfully yielding the mean $C_{10}$ and $C_{20}$ material coefficients for the muscularis (6.41±0.60, 4.29±1.87 kPa), submucosal (5.21±0.57, 3.68±3.01 kPa) and mucosal layers (0.06±0.02, 0.09±0.24 kPa). As part of the future work, we intend to identify the *in vivo* layer-specific material properties of porcine gastric tissue in addition to accounting for the anisotropy, residual strains and inhomogeneity known to be present in *in vivo* tissue.

## Acknowledgment

We gratefully acknowledge the support of this work through NIH/NIBIB 2R01EB005807, 5R01EB010037, 1R01EB009362 and 1R01EB014305. The first author acknowledges multiple discussions with Dr. Rahul over the course of the development of the hardware and software technique.

## References

[1]. Gregersen H and Kassab G, “Biomechanics of the gastrointestinal tract,” Neurogastroenterol. Motil, vol. 8, no. 4, pp. 277–297, 1996. [PubMed: 8959733]

[2]. Hirst G and Ward S, “Interstitial cells: involvement in rhythmicity and neural control of gut smooth muscle,” J. Physiol, vol. 550, no. 2, pp. 337–346, 2003. [PubMed: 12794179]

[3]. Kalloo AN et al., “Flexible transgastric peritoneoscopy: a novel approach to diagnostic and therapeutic interventions in the peritoneal cavity,” Gastrointest. Endosc, vol. 60, no. 1, pp. 114–117, Jul. 2004. [PubMed: 15229442]

[4]. Ahn W et al., “Development of a Virtual Reality Simulator for Natural orifice Translumenal Endoscopic surgery (NOTES) Cholecystectomy Procedure,” Med. Meets Virtual Real. 21 NextMedMMVR21, vol. 196, p. 1, 2014.

[5]. Gotoda T, Yamamoto H, and Soetikno RM, “Endoscopic submucosal dissection of early gastric cancer,” J. Gastroenterol, vol. 41, no. 10, pp. 929–942, 2006. [PubMed: 17096062]

[6]. Oyama T et al., “Endoscopic submucosal dissection of early esophageal cancer,” Clin. Gastroenterol. Hepatol, vol. 3, no. 7, pp. S67–S70, 2005. [PubMed: 16013002]

[7]. McMahon BP et al., “Distensibility testing of the esophagus,” Ann. N. Y. Acad. Sci, vol. 1232, no. 1, pp. 331–340, Sep. 2011. [PubMed: 21950823]

[8]. Patel RS and Rao SSC, “Biomechanical and sensory parameters of the human esophagus at four levels,” Am. J. Physiol. - Gastrointest. Liver Physiol, vol. 275, no. 2, pp. G187–G191, Aug. 1998.

[9]. Rao SS, Hayek B, and Summers RW, “Impedance planimetry: an integrated approach for assessing sensory, active, and passive biomechanical properties of the human esophagus,” Am. J. Gastroenterol, vol. 90, no. 3, pp. 431–438, Mar. 1995. [PubMed: 7872283]

[10]. Villadsen GE, Storkholm JH, Hendel L, Vilstrup H, and Gregersen H, “Impedance planimetric characterization of esophagus in systemic sclerosis patients with severe involvement of esophagus,” Dig. Dis. Sci, vol. 42, no. 11, pp. 2317–2326, 1997. [PubMed: 9398812]

[11]. Kwiatek MA, Hirano I, Kahrilas PJ, Rothe J, Luger D, and Pandolfino JE, “Mechanical properties of the esophagus in eosinophilic esophagitis,” Gastroenterology, vol. 140, no. 1, pp. 82–90, 2011. [PubMed: 20858491]

[12]. Assentoft JE, Gregersen H, and O’brien WD, “Determination of Biomechanical Properties in Guinea Pig Esophagus by Means of High Frequency Ultrasound andImpedance Planimetry,” Dig. Dis. Sci, vol. 45, no. 7, pp. 1260–1266, Jul. 2000. [PubMed: 10961701]

[13]. Takeda T, Nabae T, Kassab G, Liu J, and Mittal RK, “Oesophageal wall stretch: the stimulus for distension induced oesophageal sensation,” Neurogastroenterol. Motil, vol. 16, no. 6, pp. 721–728, Dec. 2004. [PubMed: 15601421]

[14]. Jorgensen CS, Dall FH, Jensen SL, and Gregersen H, “A new combined high-frequency ultrasound-impedance planimetry measuring system for the quantification of organ wall biomechanics in vivo,” J. Biomech, vol. 28, no. 7, pp. 863–867, Jul. 1995. [PubMed: 7657684]

[15]. Sokolis DP, Orfanidis IK, and Peroulis M, “Biomechanical testing and material characterization for the rat large intestine: regional dependence of material parameters,” Physiol. Meas, vol. 32, no. 12, p. 1969, Dec. 2011. [PubMed: 22056976]

[16]. Higa M, Luo Y, Okuyama T, Takagi T, Shiraishi Y, and Yambe T, “Passive mechanical properties of large intestine under in vivo and in vitro compression,”Med. Eng. Phys, vol. 29, no. 8, pp. 840–844, Oct. 2007. [PubMed: 17067843]

[17]. Diridollou S et al., “In vivo model of the mechanical properties of the human skin under suction,” Skin Res. Technol, vol. 6, no. 4, pp. 214–221, 2000. [PubMed: 11428960]

[18]. Evans SL and Holt CA, “Measuring the mechanical properties of human skin in vivo using digital image correlation and finite element modelling,” J. Strain Anal. Eng. Des, vol. 44, no. 5, pp. 337–345, 2009.

[19]. Veronda D and Westmann R, “Mechanical characterization of skin—finite deformations,” J. Biomech, vol. 3, no. 1, pp. 111–124, 1970. [PubMed: 5521524]

[20]. Agache P, Monneur C, Leveque J, and De Rigal J, “Mechanical properties and Young’s modulus of human skin in vivo,” Arch. Dermatol. Res, vol. 269, no. 3, pp. 221–232, 1980. [PubMed: 7235730]

[21]. Boyer G, Mattei CP, Molimard J, Pericoi M, Laquieze S, and Zahouani H, “Non contact method for in vivo assessment of skin mechanical properties for assessing effect of ageing,” Med. Eng. Phys, vol. 34, no. 2, pp. 172–178, 2012. [PubMed: 21807547]

[22]. Peterson LH, Jensen RE, and Parnell J, “Mechanical properties of arteries in vivo,” Circ. Res, vol. 8, no. 3, pp. 622–639, 1960.

[23]. Hayashi K, Handa H, Nagasawa S, Okumura A, and Moritake K, “Stiffness and elastic behavior of human intracranial and extracranial arteries,” J. Biomech, vol. 13, no. 2, pp. 175–184, 1980. [PubMed: 7364778]

[24]. Karimi A, Navidbakhsh M, Shojaei A, and Faghihi S, “Measurement of the uniaxial mechanical properties of healthy and atherosclerotic human coronary arteries,” Mater. Sci. Eng. C, vol. 33, no. 5, pp. 2550–2554, 2013.

[25]. Karimi A, Navidbakhsh M, Rezaee T, and Hassani K, “Measurement of the circumferential mechanical properties of the umbilical vein: experimental and numerical analyses,” Comput. Methods Biomech. Biomed. Engin, vol. 18, no. 13, pp. 1418–1426, 2015. [PubMed: 24773299]

[26]. Kamenskiy AV et al., “Biaxial mechanical properties of the human thoracic and abdominal aorta, common carotid, subclavian, renal and common iliac arteries,” Biomech. Model. Mechanobiol, vol. 13, no. 6, pp. 1341–1359, 2014. [PubMed: 24710603]

[27]. Yassi R, Cheng LK, Rajagopal V, Nash MP, Windsor JA, and Pullan AJ, “Modeling of the mechanical function of the human gastroesophageal junction using an anatomically realistic three-dimensional model,” J. Biomech, vol. 42, no. 11, pp. 1604–1609, Aug. 2009. [PubMed: 19481212]

[28]. Jia Z, Li W, and Zhou Z, “Mechanical characterization of stomach tissue under uniaxial tensile action,” J. Biomech, vol. 48, no. 4, pp. 651–658, 2015. [PubMed: 25596630]

[29]. Zhao J, Liao D, Chen P, Kunwald P, and Gregersen H, “Stomach stress and strain depend on location, direction and the layered structure,” J. Biomech, vol. 41, no. 16, pp. 3441–3447, Dec. 2008. [PubMed: 19004444]

[30]. Stavropoulou EA, Dafalias YF, and Sokolis DP, “Biomechanical and histological characteristics of passive esophagus: Experimental investigation and comparative constitutive modeling,” J. Biomech, vol. 42, no. 16, pp. 2654–2663, Dec. 2009. [PubMed: 19766221]

[31]. Natali AN, Carniel EL, and Gregersen H, “Biomechanical behaviour of oesophageal tissues: Material and structural configuration, experimental data and constitutive analysis,” Med. Eng. Phys, vol. 31, no. 9, pp. 1056–1062, Nov. 2009. [PubMed: 19651531]

[32]. Tottrup A, Forman A, Uldbjerg N, Funch-Jensen P, and Andersson KE, “Mechanical properties of isolated human esophageal smooth muscle,” Am. J. Physiol.-Gastrointest. Liver Physiol, vol. 258, no. 3, pp. G338–G343, 1990.

[33]. Sommer G et al., “Multiaxial mechanical response and constitutive modeling of esophageal tissues: Impact on esophageal tissue engineering,” Acta Biomater, vol. 9, no. 12, pp. 9379–9391, Dec. 2013. [PubMed: 23933485]

[34]. Yang J, Zhao J, Liao D, and Gregersen H, “Biomechanical properties of the layered oesophagus and its remodelling in experimental type-1 diabetes,” J. Biomech, vol. 39, no. 5, pp. 894–904, 2006. [PubMed: 16488228]

[35]. Fan Y, Gregersen H, and Kassab GS, “A two-layered mechanical model of the rat esophagus. Experiment and theory,” Biomed. Eng. OnLine, vol. 3, no. 1, p. 40, Nov. 2004. [PubMed: 15518591]

[36]. Stavropoulou EA, Dafalias YF, and Sokolis DP, “Biomechanical behavior and histological organization of the three-layered passive esophagus as a function of topography,” Proc. Inst. Mech. Eng. [H], vol. 226, no. 6, pp. 477–490, Jun. 2012.

[37]. Lu X and Gregersen H, “Regional distribution of axial strain and circumferential residual strain in the layered rabbit oesophagus,” J. Biomech, vol. 34, no. 2, pp. 225–233, Feb. 2001. [PubMed: 11165287]

[38]. Jorgensen C, Assentoft J, Knauss D, Gregersen H, and Briggs G, “Small intestine wall distribution of elastic stiffness measured with 500 MHz scanning acoustic microscopy,” Ann. Biomed. Eng, vol. 29, no. 12, pp. 1059–1063, 2001. [PubMed: 11853256]

[39]. Frokj^r JB, Andersen SD, Drewes AM, and Gregersen H, “Ultrasound-determined geometric and biomechanical properties of the human duodenum,” Dig. Dis. Sci, vol. 51, no. 9, pp. 1662–1669, 2006. [PubMed: 16927153]

[40]. Bader DL and Bowker P, “Mechanical characteristics of skin and underlying tissues in vivo,” Biomaterials, vol. 4, no. 4, pp. 305–308, Oct. 1983. [PubMed: 6640059]

[41]. Hendriks FM, Brokken D, Oomens CWJ, Bader DL, and Baaijens FPT, “The relative contributions of different skin layers to the mechanical behavior of human skin in vivo using suction experiments,” Med. Eng. Phys, vol. 28, no. 3, pp. 259–266, Apr. 2006. [PubMed: 16099191]

[42]. Palmeri M et al., “Acoustic radiation force impulse (ARFI) imaging of the gastrointestinal tract,” presented at the Ultrasonics Symposium, 2004 IEEE, 2004, vol. 1, pp. 744–747.

[43]. Gregersen H et al., “Mechanical properties in the human gastric antrum using B-mode ultrasonography and antral distension,” Am. J. Physiol.-Gastrointest. Liver Physiol, vol. 283, no. 2, pp. G368–G375, 2002. [PubMed: 12121884]

[44]. Kauer M, “Inverse finite element characterization of soft tissues with aspiration experiments,” ETH Zür. Swiss Fed. Inst. Technol. Zür. Switz, 2001.

[45]. Brown JD, Rosen J, Kim YS, Chang L, Sinanan MN, and Hannaford B, “In-vivo and in-situ compressive properties of porcine abdominal soft tissues,” Stud. Health Technol. Inform, pp. 26–32, 2003. [PubMed: 15455858]

[46]. Ottensmeyer MP, Kerdok AE, Howe RD, and Dawson SL, “The effects of testing environment on the viscoelastic properties of soft tissues,” in Medical Simulation, Springer, 2004, pp. 9–18.

[47]. Ophir J, Céspedes I, Ponnekanti H, Yazdi Y, and Li X, “Elastography: A quantitative method for imaging the elasticity of biological tissues,” Ultrason. Imaging, vol. 13, no. 2, pp. 111–134, Apr. 1991. [PubMed: 1858217]

[48]. Maurice RL, Daronat M, Ohayon J, Stoyanova E, Foster FS, and Cloutier G, “Non-invasive high-frequency vascular ultrasound elastography,” Phys. Med. Biol, vol. 50, no. 7, p. 1611, 2005. [PubMed: 15798347]

[49]. Zheng Yong-Ping and Mak AFT, “An ultrasound indentation system for biomechanical properties assessment of soft tissues in-vivo,” Biomed. Eng. IEEE Trans. On, vol. 43, no. 9, pp. 912–918, 1996.

[50]. Liang X and Boppart S, “Biomechanical properties of in vivo human skin from dynamic optical coherence elastography,” Biomed. Eng. IEEE Trans. On, vol. 57, no. 4, pp. 953–959, 2010.

[51]. Cespedes I, Ophir J, Ponnekanti H, and Maklad N, “Elastography: Elasticity Imaging Using Ultrasound with Application to Muscleand Breast In Vivo,” Ultrason. Imaging, vol. 15, no. 2, pp. 73–88, Apr. 1993. [PubMed: 8346612]

[52]. Varghese T, Zagzebski J, Frank G, and Madsen E,”Elastographic imaging using a handheld compressor,” Ultrason. Imaging, vol. 24, no. 1, pp. 25–35, 2002. [PubMed: 12102226]

[53]. Souchon R et al., “Visualisation of HIFU lesions using elastography of the human prostate in vivo: preliminary results,” Ultrasound Med. Biol, vol. 29, no. 7, pp. 1007–1015, 2003. [PubMed: 12878247]

[54]. Lindop JE, Treece GM, Gee AH, and Prager RW, “3D elastography using freehand ultrasound,” Ultrasound Med. Biol, vol. 32, no. 4, pp. 529–545, 2006. [PubMed: 16616600]

[55]. Doyley MM, Bamber JC, Fuechsel F, and Bush NL, “A freehand elastographic imaging approach for clinical breast imaging: system development and performance evaluation,” Ultrasound Med. Biol, vol. 27, no. 10, pp. 1347–1357, 2001. [PubMed: 11731048]

[56]. Zhao J, Liao D, and Gregersen H, “Tension and stress in the rat and rabbit stomach are location- and direction-dependent,” Neurogastroenterol. Motil, vol. 17, no. 3, pp. 388–398, Jun. 2005. [PubMed: 15916626]

[57]. Barbone PE and Gokhale NH, “Elastic modulus imaging: on the uniqueness and nonuniqueness of the elastography inverse problem in two dimensions,” Inverse Probl, vol. 20, no. 1, p. 283, 2004.

[58]. Byrd RH, Schnabel RB, and Shultz GA, “Approximate solution of the trust region problem by minimization over two-dimensional subspaces,” Math. Program, vol. 40, no. 1–3, pp. 247–263, 1988.

[59]. Speirs D, de Souza Neto E, and Peric D, “An approach to the mechanical constitutive modelling of arterial tissue based on homogenization and optimization,” J. Biomech, vol. 41, no. 12, pp. 2673–2680, 2008. [PubMed: 18674766]

[60]. Davis FM and De Vita R, “A nonlinear constitutive model for stress relaxation in ligaments and tendons,” Ann. Biomed. Eng, vol. 40, no. 12, pp. 2541–2550, 2012. [PubMed: 22648576]

[61]. Zhong Q, Zeng W, Fluang X, Su M, and Luo Y, “Constitutive modeling and finite element analysis of myxomatous mitral leaflet tissue,” J. Mech. Med. Biol, vol. 14, no. 03, p. 1450031, 2014.

[62]. Martins P, Natal Jorge R, and Ferreira A, “A Comparative Study of Several Material Models for Prediction of Flyperelastic Properties: Application to SiliconeDRubber and Soft Tissues,” Strain, vol. 42, no. 3, pp. 135–147, 2006.

[63]. Kim J and Srinivasan MA, “Characterization of viscoelastic soft tissue properties from in vivo animal experiments and inverse FE parameter estimation,” in Medical Image Computing and Computer-Assisted Intervention—MICCAI 2005, Springer, 2005, pp. 599–606.

[64]. Kauer M, Vuskovic V, Dual J, Szekely G, and Bajka M, “Inverse finite element characterization of soft tissues,” Spec. Issue Med. Image Comput. Comput.-Assist. Interv. - MICCAI 2001, vol. 6, no. 3, pp. 275–287, Sep. 2002.

[65]. Vanden Berghen F, “CONDOR: a constrained, non-linear, derivative-free parallel optimizer for continuous, high computing load, noisy objective functions.,” 2004.

[66]. Manickam K, Machireddy RR, and Seshadri S, “Study of ultrasound stiffness imaging methods using tissue mimicking phantoms,” Ultrasonics, vol. 54, no. 2, pp. 621–631, 2014. [PubMed: 24083832]

[67]. Manickam K, Machireddy RR, and Seshadri S, “Characterization of biomechanical properties of agar based tissue mimicking phantoms for ultrasound stiffness imaging techniques,” J. Mech. Behav. Biomed. Mater, vol. 35, pp. 132–143, 2014. [PubMed: 24769915]

[68]. Flail TJ, Bilgen M, Insana MF, and Krouskop T, “Phantom materials for elastography,” Ultrason. Ferroelectr. Freq. Control IEEE Trans. On, vol. 44, no. 6, pp. 1355–1365, 1997.

[69]. Klein S, Staring M, Murphy K, Viergever M, and Pluim JP, “Elastix: a toolbox for intensity-based medical image registration,” Med. Imaging IEEE Trans. On, vol. 29, no. 1, pp. 196–205, 2010.

[70]. Fung Y, “Biomechanics: mechanical properties of living tissues. 1993.”

[71]. Krouskop TA, Wheeler TM, Kallel F, Garra BS, and Flail T, “Elastic moduli of breast and prostate tissues under compression,” Ultrason. Imaging, vol. 20, no. 4, pp. 260–274, 1998. [PubMed: 10197347]

[72]. Ottensmeyer MP and Salisbury JK, Jr, “In vivo data acquisition instrument for solid organ mechanical property measurement,” presented at the International Conference on Medical Image Computing and Computer-Assisted Intervention, 2001, pp. 975–982.

[73]. DeKosky BJ et al., “Hierarchically designed agarose and poly (ethylene glycol) interpenetrating network hydrogels for cartilage tissue engineering,” Tissue Eng. Part CMethods, vol. 16, no. 6, pp. 1533–1542, 2010.

[74]. Parker KJ and Lyons ME, “Absorption and attenuation in soft tissues. I. Calibration and error analyses,” IEEE Trans. Ultrason. Ferroelectr. Freq. Control, vol. 35, no. 2, pp. 242–252, 1988. [PubMed: 18290150]

[75]. Hewick S, Fairhead A, Culy J, and Atta H, “A comparison of 10 MHz and 20 MHz ultrasound probes in imaging the eye and orbit,” Br. J. Ophthalmol, vol. 88, no. 4, pp. 551–555, 2004. [PubMed: 15031175]

[76]. Staring M, Klein S, Reiber JH, Niessen WJ, and Stoel BC, “Pulmonary image registration with elastix using a standard intensity-based algorithm,” Book Pulm. Image Regist. Elastix Using Stand. Intensity-Based Algorithm, 2010.

[77]. Wheater PR and Young B, Wheater’s functional histology: a text and colour atlas. Churchill Livingstone, 2006.

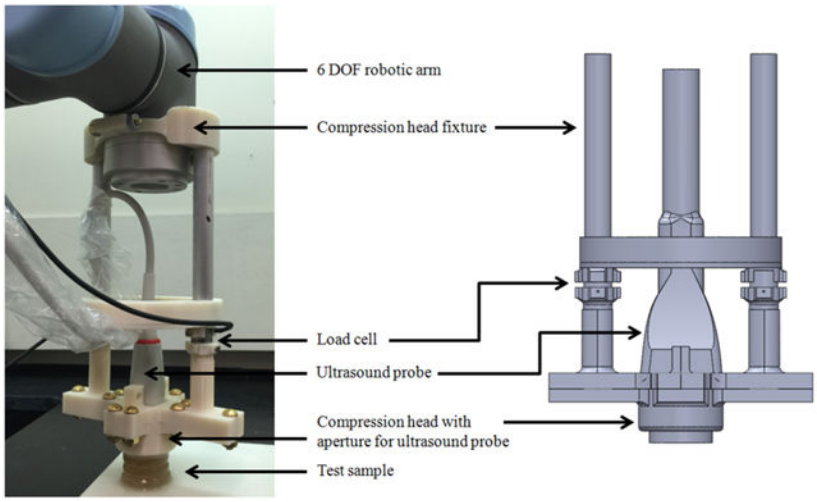


**Fig. 1.**
The Soft Tissue Elastography Robotic Arm (STiERA)

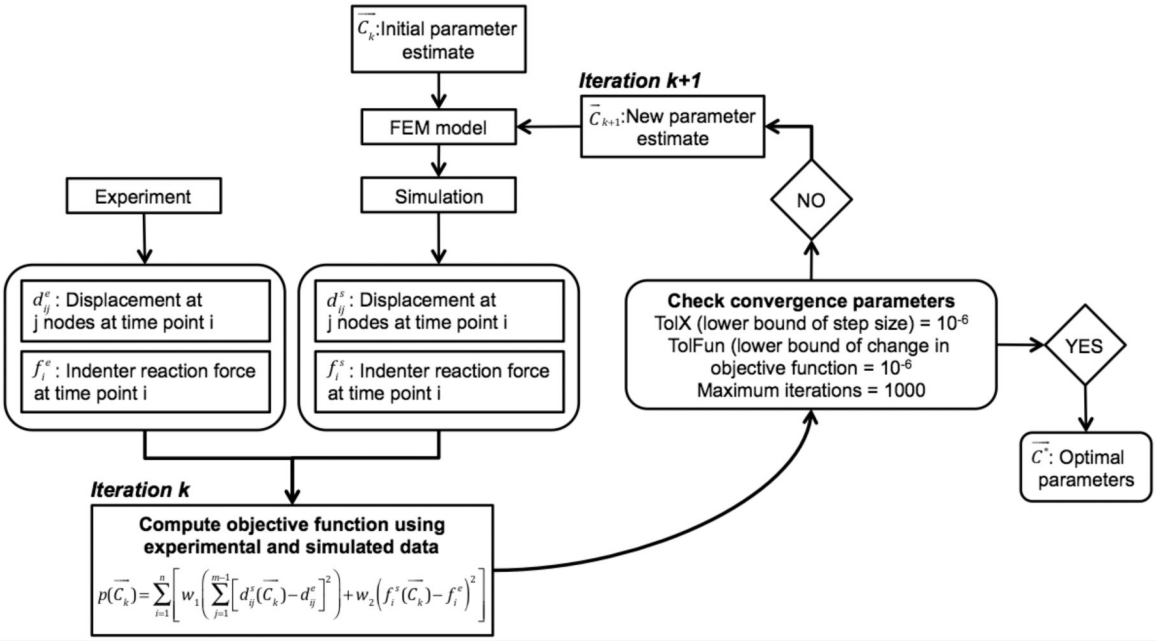


**Fig. 2.**

A flowchart detailing the algorithm for the iterative optimization of the material coefficients

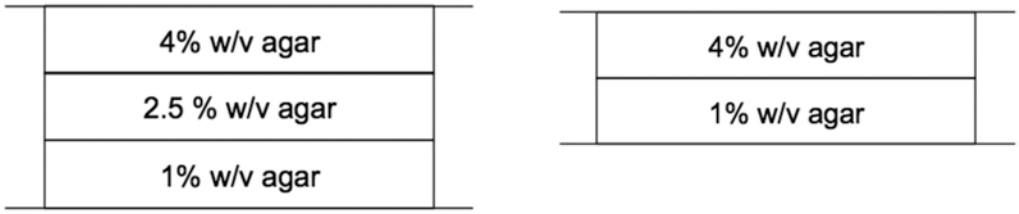


**Fig. 3.**
Composition of the three layer (left) and two-layer (right) agar gel test samples

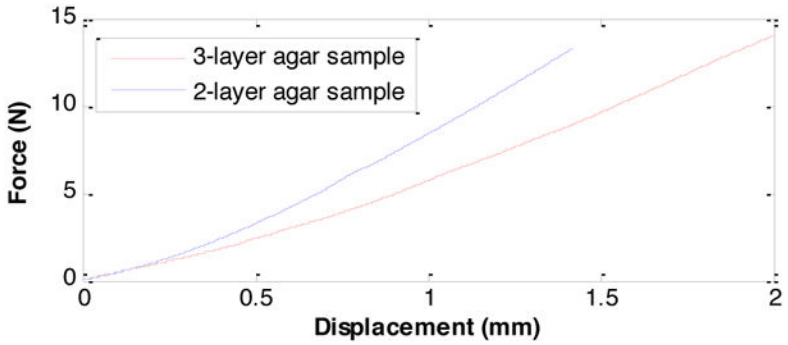


**Figure 4.**

The force signal from the STiERA system in response to 20% compression for a representative 2 and 3-layer agar gel phantom.

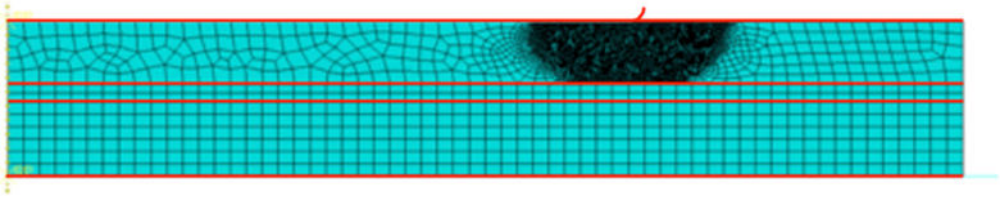

**Fig. 5.**

The three-layer geometry of an *ex vivo* porcine sample with the indenter on the top surface (darker area on the top layer shows region of high mesh density to account for edge effects of the indenter)

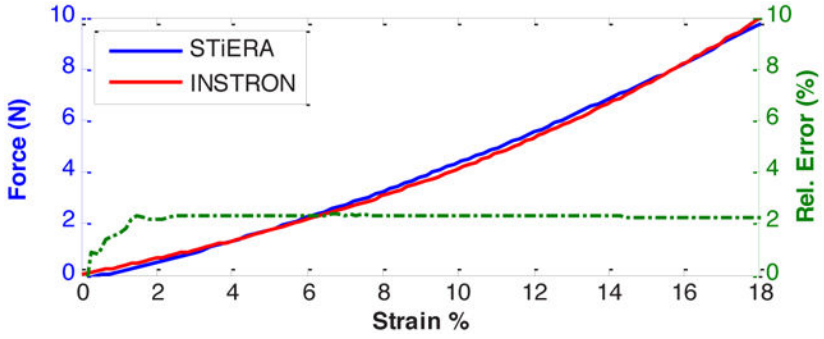


**Figure 6.**

The comparison of the force signals from Instron® MTS and the STiERA for the single layer 2.5% agar sample with the relative error %.

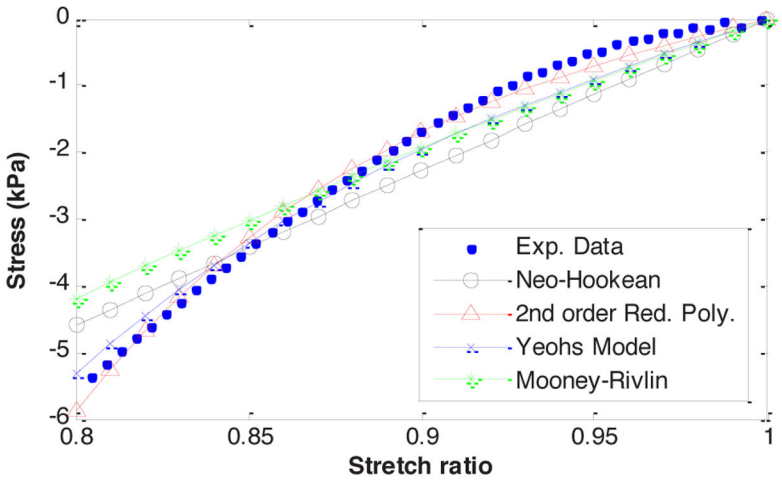


**Fig.7.**

The fit of the hyperelastic models to the single layer experimental data for the 2.5% w/v concentration sample up to 20% compressive strain (stretch ratio 0.8)

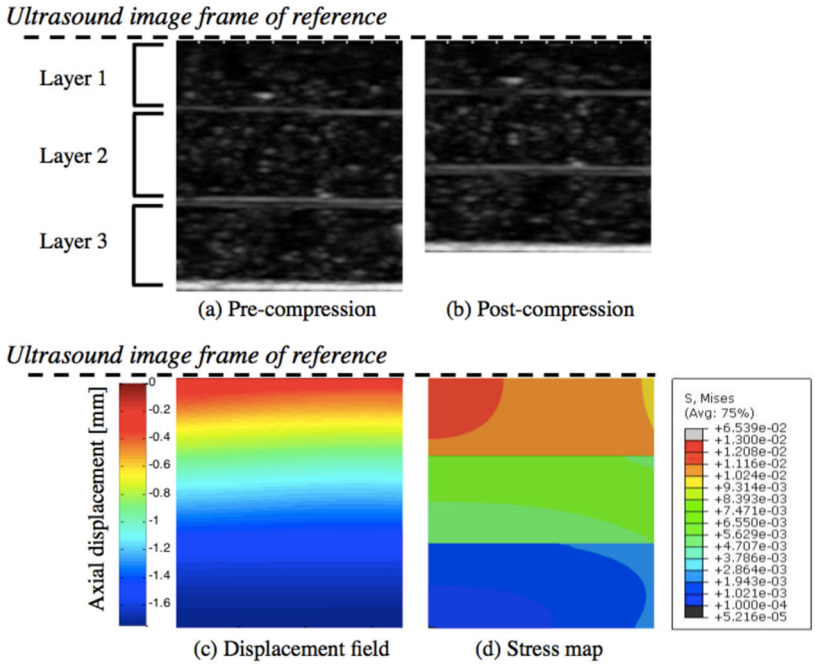


**Fig. 8.**

The (a) 8mm deep and 7.3mm wide pre-compression and (b) post-compression B-mode ultrasound image of a 3-layer agar gel sample with the (c) displacement field calculated using the *elastix* image registration toolkit as well as the (d) stress map obtained from the finite element simulation

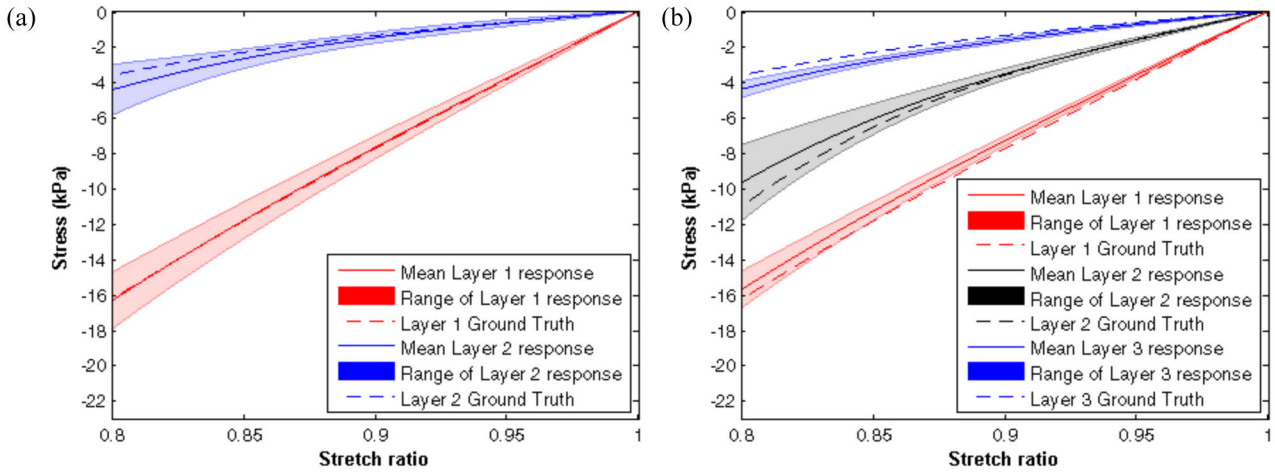


**Fig. 9.**

A comparison of the STiERA based system material model for each layer and the INSTRON determined ground truth model for the (a) 2-layer and (b) 3-layer agar gel sample. The range corresponding to a layer's response highlights the variation in material response of that layer over three different multi-layer samples tested three times each.

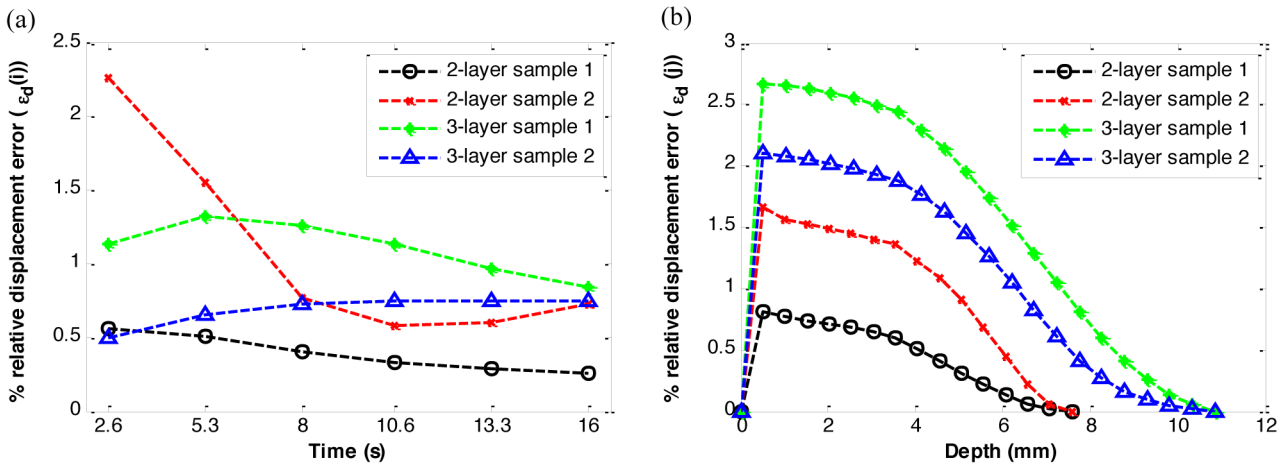


**Fig. 10.**

The % relative displacement error between the experimental and optimized model of (a) 2 and 3-layer samples over six time steps (b) the % relative displacement error along the depth of the sample (the markers indicate nodes where computations were performed)

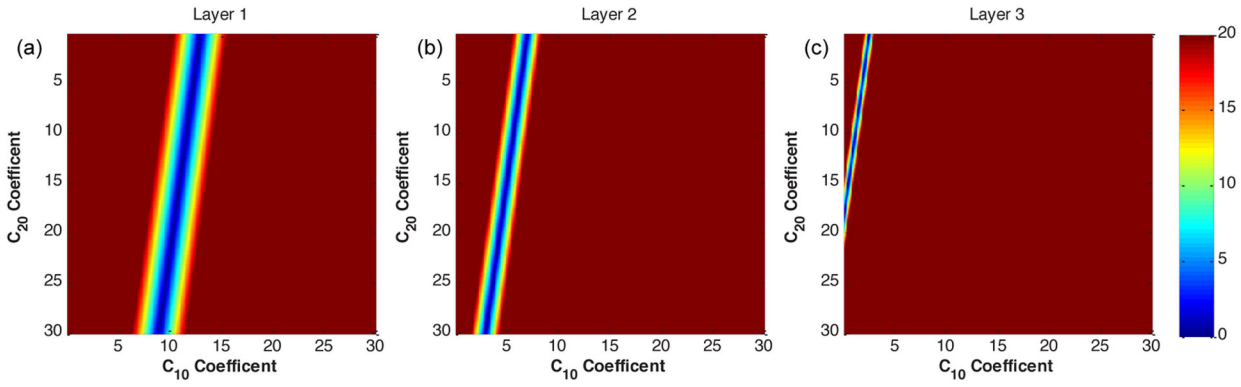


**Fig.11.**

The sensitivity maps of the solutions for each of the three stiffness layers (a) 4%, (b) 2.5% and (c) 1% w/v expressed in terms of the % relative error of strain energy when compared to their respective ground-truth models (coefficients in kPa)

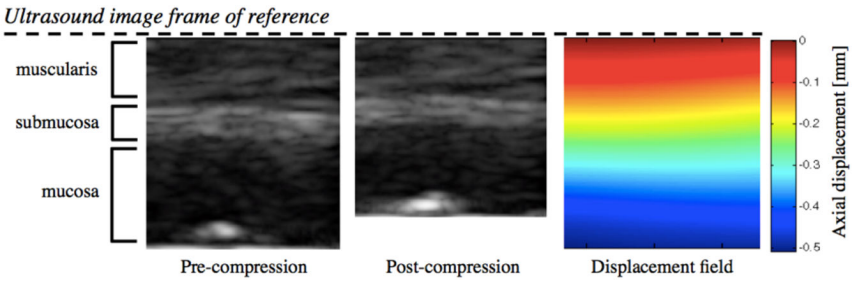


**Fig. 12.**

Axial displacement field obtained from the pre- and post-compression B-mode ultrasound images of *ex vivo* porcine gastric tissue using the *elastix* image registration toolkit

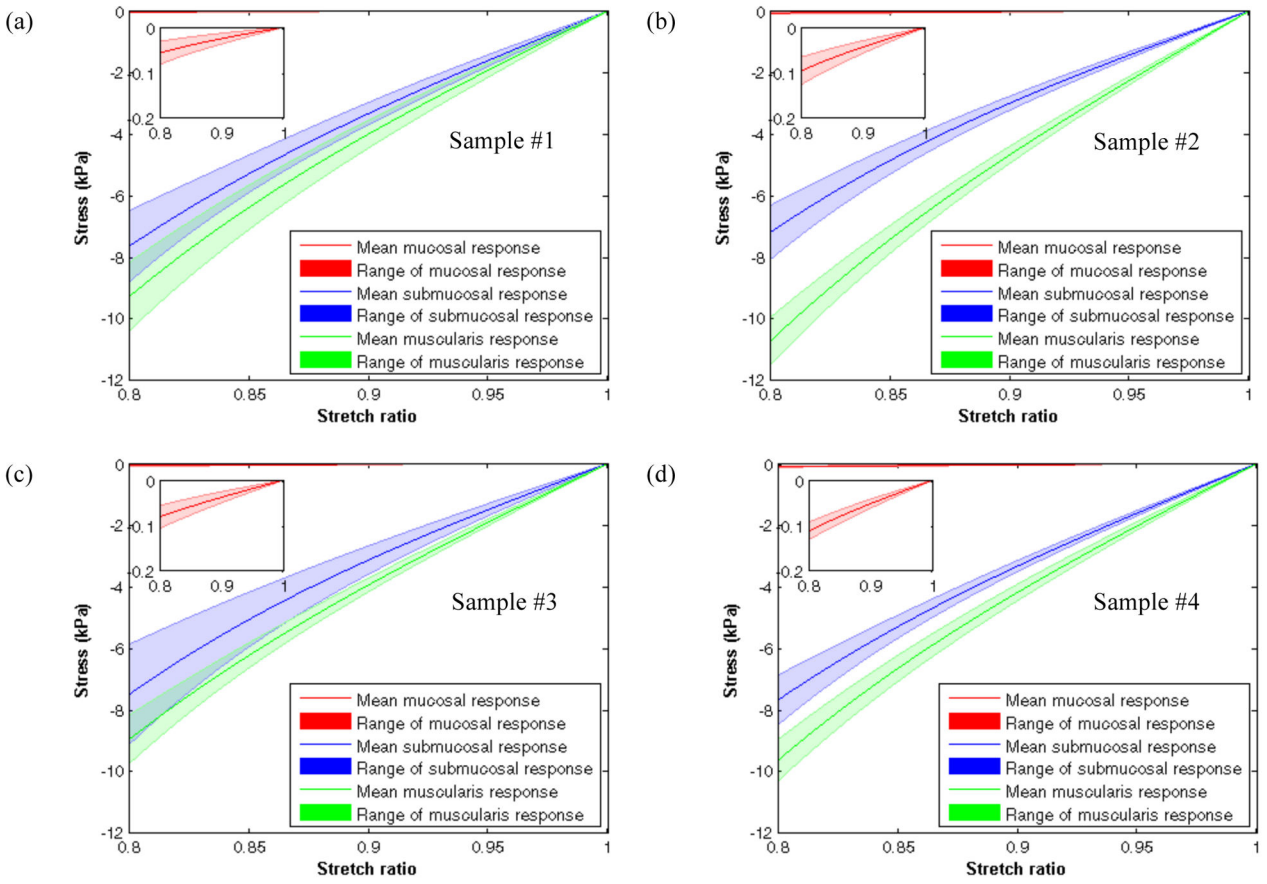


**Fig. 13.**

The range of layer-specific material properties identified using the STiERA system for porcine *ex vivo* (a) sample #1, (b) sample #2, (c) sample #3 and (d) sample #4.

**TABLE 1**

The strain energy density function (W) and Cauchy stress ($\sigma_1$) for four hyperelastic material models

| |
|---|
| ***Neo-Hookean*** |
| $W = C_{10}(I_1 - 3)$ |
| $\sigma_1 = 2C_{10}\left(\lambda_1^2 - \frac{1}{\lambda_1}\right)$ |
| ***Mooney-Rivlin*** |
| $W = C_{10}(I_1 - 3) + C_{01}(I_2 - 3)$ |
| $\sigma_1 = \left(\lambda_1^2 - \frac{1}{\lambda_1}\right)\left(2C_{10} + \frac{2C_{01}}{\lambda_1}\right)$ |
| ***2nd order reduced polynomial*** |
| $W = C_{10}(I_1 - 3) + C_{20}(I_1 - 3)^2$ |
| $\sigma_1 = 2\left(\lambda_1^2 - \frac{1}{\lambda_1}\right)\left(C_{10} + 2C_{20}\left(\frac{2}{\lambda_1} + \lambda_1^2 - 3\right)\right)$ |
| ***Yeoh Model (3rd order reduced polynomial)*** |
| $W = C_{10}(I_1 - 3) + C_{20}(I_1 - 3)^2 + C_{30}(I_1 - 3)^3$ |
| $\sigma_1 = 2\left(\lambda_1^2 - \frac{1}{\lambda_1}\right)\left(C_{10} + 2C_{20}\left(\lambda_1^2 - \frac{1}{\lambda_1}\right) + 3C_{30}\left(\lambda_1^2 - \frac{1}{\lambda_1}\right)^2\right)$ |

**TABLE 2**

The default settings for the Matlab® curve fitting toolbox when using trust-region-reflective optimization

| Parameter | Description | Setting |
|---|---|---|
| Startpoint | Initial guess of coefficients | Random |
| DiffMaxChange | Max change in coefficient | $10^{-6}$ |
| DiffMinChange | Min change in coefficient | $10^{-6}$ |
| MaxFunEvals | Max number of model evaluations | 600 |
| MaxIter | Max number of iterations for fitting | 1000 |
| TolFun | Termination tolerance on obj. function | $10^{-6}$ |
| TolX | Termination tolerance on coeff. values | $10^{-6}$ |

**TABLE 3**

The NRMSE value of each model for all three concentrations of agar gel samples

| Agar Sample Concentration | Neo-Hookean | Mooney-Rivlin | 2nd order red poly | Yeoh |
|---|---|---|---|---|
| 1% w/v | 3.942% | 1.523% | 0.732% | 0.732% |
| 2.5% w/v | 6.982% | 4.766% | 1.763% | 1.763% |
| 4% w/v | 3.394% | 1.044% | 0.853% | 0.853% |

**TABLE 4**

The ground-truth values for each concentration of agar gel as determined by Instron® MTS testing

| Agar Sample Concentration | $C_{10}$ (kPa) | $C_{20}$ (kPa) |
|---|---|---|
| 1% w/v | 2.10 ±0.05 | 3.10 ±0.14 |
| 2.5% w/v | 5.10 ±0.27 | 14.01 ±0.60 |
| 4% w/v | 12.70 ±0.48 | 2.10 ±0.08 |

**TABLE 5**

Mean (±standard deviation) of the C10 and C20 coefficient values (kPa) computed for layers of the four porcine stomach samples

| Sample number | Muscularis | | Submucosa | | Mucosa | |
|---|---|---|---|---|---|---|
| | $C_{10}$ | $C_{20}$ | $C_{10}$ | $C_{20}$ | $C_{10}$ | $C_{20}$ |
| 1 | 6.35±0.74 | 4.49±2.04 | 5.31±0.63 | 3.40±3.37 | 0.05±0.02 | 0.10±0.29 |
| 2 | 7.45±0.46 | 4.79±1.84 | 4.71±0.34 | 4.26±2.25 | 0.07±0.02 | 0.03±0.02 |
| 3 | 6.30±0.36 | 3.73±2.08 | 4.92±0.62 | 4.39±3.08 | 0.06±0.02 | 0.08±0.22 |
| 4 | 6.65±0.44 | 4.43±1.35 | 5.30±0.29 | 3.55±2.37 | 0.08±0.01 | 0.08±0.18 |
| Overall mean (±std. dev.) | 6.68±0.52 | 4.36±1.85 | 5.06±0.49 | 3.90±2.80 | 0.06±0.01 | 0.07±0.20 |